RESEARCH ARTICLE | OCTOBER 25 2023

Structure evolution of the interfacial layer of BaTiO₃ thin films during annealing process and related good resistive switching behaviors

Zixiong Sun (孙梓雄) ✉ 🔟 ; Sizhao Huang 🔟 ; Wenxuan Zhu; Yorick A. Birkhölzer 🔟 ; Xing Gao (兴) 🔟 ;
Romar Angelo Avila; Houbing Huang ✉ 🔟 ; Xiaojie Lou 🔟 ; Evert P. Houwman 🔟 ; Minh D. Nguyen ✉ 🔟 ;
Gertjan Koster 🔟 ; Guus Rijnders ✉

Check for updates

View Online   Export Citation   CrossMark

Structure evolution of the interfacial layer of BaTiO₃ thin films during annealing process and related good resistive switching behaviors

Zixiong Sun (孙梓雄),[1,2,a] Sizhao Huang,[1] Wenxuan Zhu,[3] Yorick A. Birkhölzer,[1] Xing Gao (高兴),[1]
Romar Angelo Avila,[1] Houbing Huang,[3,a] Xiaojie Lou,[4] Evert P. Houwman,[1] Minh D. Nguyen,[1,a]
Gertjan Koster,[1] and Guus Rijnders[1,a]

AFFILIATIONS

[1] MESA⁺ Institute of Nanotechnology, University of Twente, P.O. Box 217, Enschede 7500 AE, The Netherlands
[2] School of Electronic Information and Artificial Intelligence, Shaanxi University of Science and Technology, Xi'an 710021, China
[3] School of Materials Science and Engineering and Advanced Research Institute of Multidisciplinary Science,
 Beijing Institute of Technology, Beijing 100081, China
[4] Frontier Institute of Science and Technology, State Key Laboratory for Mechanical Behavior of Materials,
 Xi'an Jiaotong University, Xi'an 710049, China

[a] Authors to whom correspondence should be addressed: z.x.sun@utwente.nl; hbhuang@bit.edu.cn;
 d.m.nguyen@utwente.nl; and a.j.h.m.rijnders@utwente.nl

ABSTRACT

BaTiO₃ thin films with different annealing times were grown on LSMO/STO (001) substrates by pulsed laser deposition. An interesting phenomenon of *loss-and-reappearance* of the interfacial layer in BaTiO₃ was detected in the x-ray diffraction results, and the ordered–unordered–ordered lattice transformation caused by oxygen vacancies' filling was thought to be the reason. The ferroelectric domain was also confirmed to form during such an annealing process according to the piezoresponse force microscopy, transmission electron microscopy, and phase-field simulation. A Ti-displacement-rotation region considered an intermediate structure during the domain formation was observed at the interfacial layer of the 5.5-min-annealing film. Because of the oxygen deficiency and the effect of ferroelectric domain modulation of the built-in barrier height, a good memristive behavior with a resistive switching ratio of 1916 was obtained in the 10-min-annealing BaTiO₃ (BTO) film, offering an avenue toward the application of oxygen-deficient BTO in neural network applications.

The BaTiO₃ (BTO) film is a perovskite-structured oxide with enormous applications, such as ferroelectric memristors.[1–11] Pulsed laser deposition (PLD) is one of the most common preparation methods. In most cases, an interfacial layer exists between the film and the bottom material due to lattice mismatch. In previous work, for example, those interfacial layers marked by red arrows in Fig. S1 were detected but lacked investigation. In some of them, such phenomena and related properties were partly reported: Kan and Shimakawa[12] revealed that the interfacial layer thickness of BTO can be regulated by laser fluence. Li *et al.*[13] demonstrated the existence of the interfacial layer in BTO by transmission electron microscopy (TEM); such a coating improved the film's polarization to ~70 μC/cm². Even so, the origin and evolution of the interfacial layer remain unclear. Motivated by this, we made a systematical study to uncover the formation and transformation of such an interfacial layer. In this work, the BTO films were grown on LSMO/STO (001) by PLD, and it is quite interesting that there occurred a *loss-and-reappearance* in the BTO interfacial layer during the annealing process. Such a phenomenon was believed to be caused by the ordered–unordered–ordered lattice transformation with oxygen filling into the vacancies. Meanwhile, a good resistance switching (*RS*) behavior was achieved in our film, underlining

the potential of applying oxygen-deficient BTO in neuromorphic memory devices.[14,15]

The crystallographic information of the LSMO layer (*bottom electrode*) is shown in Fig. S2. The BTO has grown coherently, and Fig. 1(a) shows this heterostructure. Figure 1(b) exhibits the evolution of real-time high-energy electron diffraction (RHEED) patterns during BTO growth. 700 pulses are required for 45 nm, and a 2D to 3D growth mode transition can be observed at ~140 shots, corresponding to ~8 nm.[16] *In situ* post-annealing (*the annealing conditions can be found in the* supplementary material) was carried out after growth. The x-ray diffraction (XRD) 2theta–ω-scans around the (002) plane of these heterostructures with different annealing times are shown in Fig. 1(b). [*A longer-range scan from* 15° *to* 55° *can be seen in* Fig. S3(a).] As expected, the BTO peak split into a main peak and a side peak. The main peak moves to a higher angle with increasing annealing time from 0 to 5.5 min and then returns after further annealing; interestingly, the side peak is lost after 5.5-min-annealing but reappears at a higher angle after longer-time annealing, demonstrating a lattice transition of the interfacial

layer of BTO. This is quite a novel phenomenon, with few studies focusing on it. We employed the Gaussian–LorenCross function as shown in Eq. (S1)[17,18] to fit such 2theta–ω data and plotted the result in Figs. 1(d1)–1(d5). For the as-grown and 3-min-annealing films, the results were both fitted with three peaks. Except for the main peak (*blue*) and side peak (*orange*), a buffer peak (*green*), which symbolizes the dislocation and lattice deformation caused by the interfacial strain,[19–21] was also fitted. The intensity of the side peak decreases with increasing annealing time and almost disappears at 5.5-min-annealing. Meanwhile, a new side peak (*purple*) with a higher 2T value is fitted out, and further increasing the annealing time improves its intensity.

Reciprocal space mappings (RSMs) around the (002) and (103) planes of these films are displayed in Figs. S4(a1)–S4(a5) and S4(b1)–S4(b5), respectively. Consistent with the 2theta–ω result, two BTO peaks can be seen in all the other four films except for the 5.5-min-annealing one. The main peaks are all relaxed, while the side peaks are all strained along LSMO/STO. Enlarged mappings around the BTO (103) plane with lattice parameters are shown
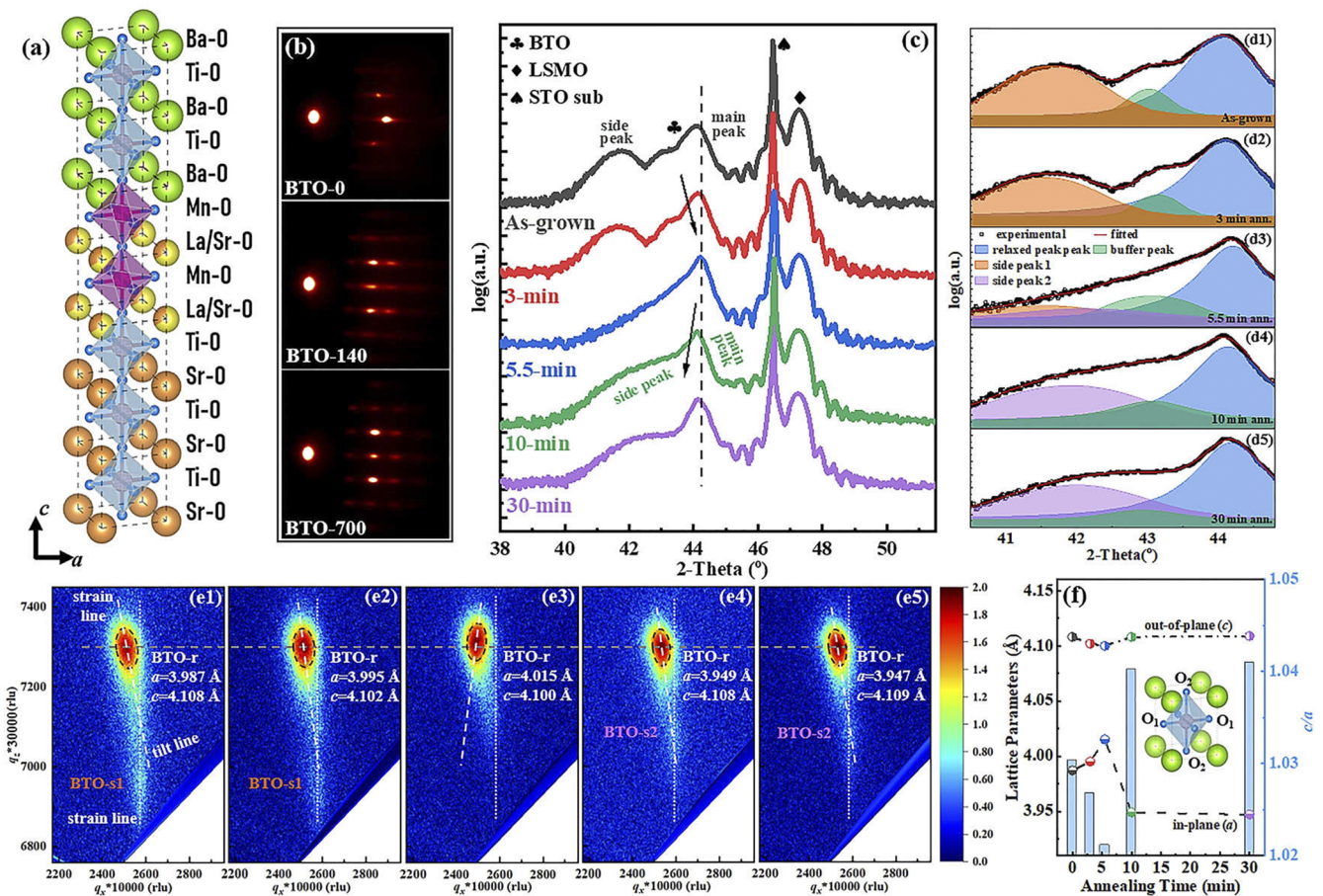
FIG. 1. (a) Sketch of the BTO grown on LSMO/STO in this work; (b) evolution of RHEED images during BTO layer growth; (c) 2theta–ω-scan around the (002) plane of BTO grown on LSMO/STO with different annealing times; (d1)–(d5) Gaussian–LorenCross fitting result of the BTO (002) plane with different annealing times; (e1)–(e5) high-resolution RSM around the BTO (103) plane with different annealing times; and (f) lattice parameter variation in BTO-r with different annealing times.

in Figs. 1(e1)–1(e5), and their variation tendencies are plotted in Fig. 1(f). Here, we define the side peak before and after 5.5-min-annealing as BTO-s1 and BTO-s2, respectively, and the main peak as BTO-r. The lattice variation in BTO-r was divided into two periods: Before 5.5 min annealing, the in-plane lattice parameter (a) increases, and the out-of-plane lattice parameter (c) decreases with increasing annealing time, while both show an opposite tendency after 5.5-min-annealing. This can be explained as follows: the BTO film suffers compress strain from LSMO, so a specific part in the bottom (BTO-s1) is inevitably strained. Such a strained layer followed a 2D mode with a thickness of ~8 nm, as mentioned above. Judging by the tilt angle of BTO-r, which points from top left to bottom right in Fig. 1(e1), BTO-r also suffers compress strain from BTO-s1 before annealing. When the annealing started, the oxygen first entered the O_1-site rather than the O_2-site due to the higher bond energy of Ti–O_1 than Ti–O_2 in T-phase BTO,[22] as shown in Fig. 1(f), resulting in an increment of a and decrement of c. Meanwhile, the interfacial strain in both BTO-r/BTO-s1 and BTO-s1/LSMO interface decreased, which probably disordered the lattice arrangement in BTO-s1 and thus lowered its XRD intensity, as

shown in Fig. 1(e2). When the annealing time reached 5.5 min, more oxygen vacancies were filled, and the a and c reached their highest and lowest values, respectively. The BTO strained layer became too unordered that no diffraction signal could be collected from XRD, leading to the loss of BTO-s1, as observed in Fig. 1(e3). Such an unordered strained layer can hardly offer interfacial strain to the relaxed layer above, so the tilt line exhibits a different angle. After the O_1-site was all filled, further annealing made the oxygens enter the O_2-site, which might increase a and decrease c of BTO simultaneously. Smaller a decreased the lattice mismatch between BTO and LSMO and strained the bottom BTO layer again, leading to the reappearance of the strained layer (BTO-s2). The reappearance of interfacial strain between BTO-r and BTO-s2 can be confirmed by the angle of the tilt line in Figs. 1(e4) and 1(e5).

The cross-sectional high-angle annular dark-field (HAADF) image of the as-grown film is shown in Fig. 2(a1). Some dislocations, which offset the lattice mismatch between BTO-r and BTO-s1,[23] can be observed in area-a and area-b. The formation of these dislocations was attributed to the high oxygen vacancy concentration[24–26] and resulted in the buffer peak as mentioned above. The corresponding
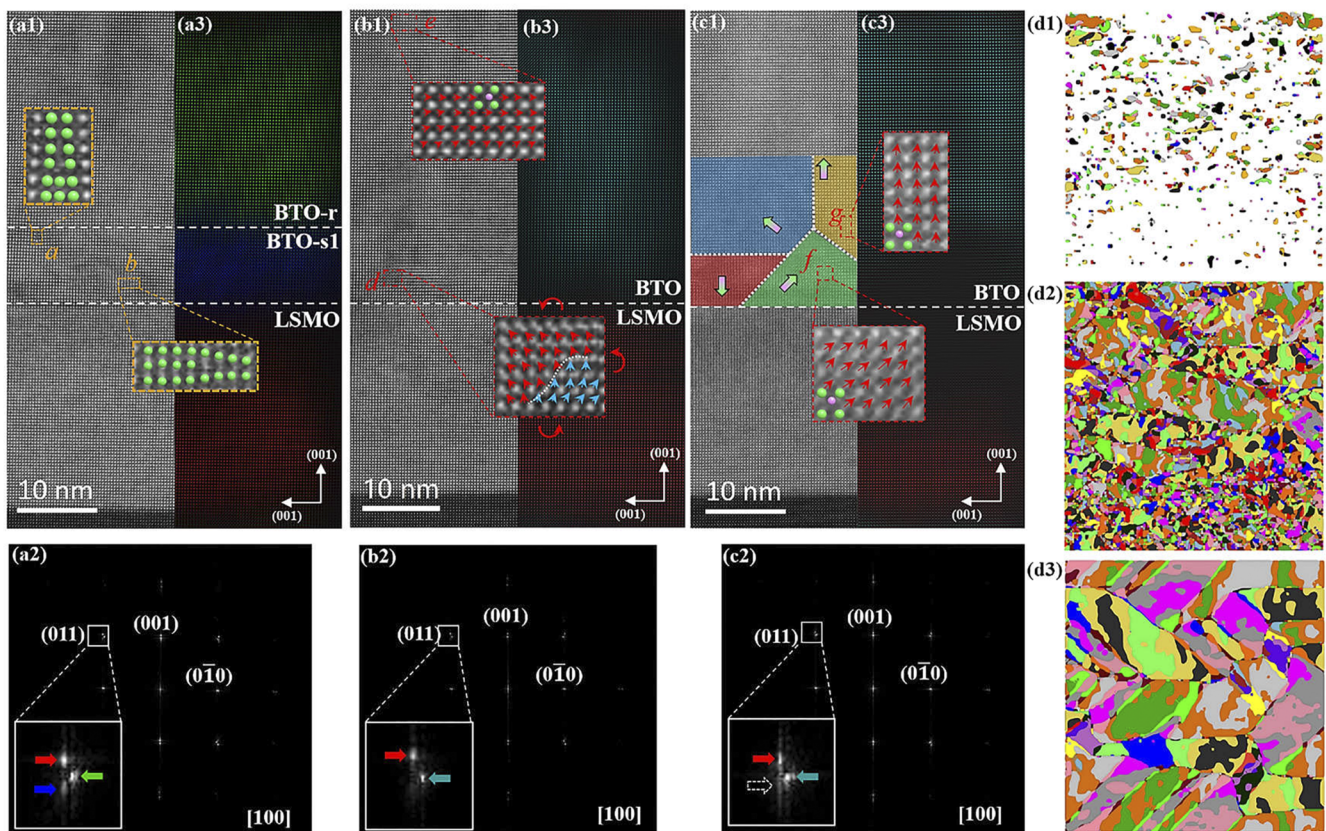
FIG. 2. (a1)–(a3) Cross-sectional HAADF, FFT, and IFT images of BTO grown on LSMO/STO without annealing; area-a and area-b show the dislocations in the strained layer. (b1)–(b3) Cross-sectional HAADF, FFT, and IFT images of BTO grown on LSMO/STO with an annealing time of 5.5 min; area-d shows the TRR at the bottom part of the film, and area-e shows the normal-sized ferroelectric domain at the top part of the film. (c1)–(c3) Cross-sectional HAADF, FFT, and IFT images of BTO grown on LSMO/STO with an annealing time of 10 min; area-f and area-g show the normal-sized ferroelectric domains based on the Ti-displacement. (d1)–(d3) Ferroelectric domain configuration in the BTO film with an annealing time of 0, 5.5, and 10 min, respectively, according to the phase field simulation.

fast Fourier transform (FFT) image along the [001] axis is displayed in Fig. 2(a2). The reflection patterns in the FFT image indicate the single crystal characteristic of the film. From the enlarged view around (011), we can see three separated reflection patterns marked with red, green, and blue arrows, representing the LSMO, BTO-r, and BTO-s1, respectively. Each pattern reflects one layer in the colored inverse Fourier transform (IFT) image in Fig. 2(a3), which matches well with the HAADF image. Figures 2(b1)–2(b3) illustrate the HAADF, FFT, and IFT images of the 5.5-min-annealing film. No interface can be distinguished in the BTO layer in either HAADF or IFT image. Similarly, from the FFT image of the 5.5-min-annealing film, we can still see the reflection patterns of LSMO and BTO-r, but the pattern of BTO-s1 disappears. Instead of dislocations, the Ti-displacement's rotation regions (TRRs) were observed at the same height, as seen in area-c, and this TRR can be divided into different "*nano ferroelectric domains*" based on Ti-displacement's orientation. The TRR is a disordered intermediate structure in the ferroelectric domain (FD) formation during annealing. It is the reason for the disappearance of both interfacial strain and the strained layer of

5.5-min-annealing film. On the top of the film, normal-sized FDs can be found as marked with area-e. When the annealing time was further increased to 10 min, we could still only see one kind of BTO layer in both HAADF and FFT images, while in the IFT image, a weak and diffused BTO-s layer can be observed. This is because the strained layer of the 10-min-annealing film consists of two different regions: Some regions are relaxed with normal-sized FDs, as shown in Fig. 2(c1), while the other regions, which are still strained, are defined as locally strained regions (LSRs), as shown in Fig. S5. For the former ones, the spontaneous polarization direction of each domain is distinguished by the Ti displacement as seen in area-f and area-g. The LSRs disperse in them and result in the BTO-s2 peak. Because of the coexistence of the relaxed regions and LSRs with a lattice tilt, as displayed in area-m and area-l in Fig. S5, the strain in the BTO-r/BTO-s2 interface can also be released without dislocations' formation. The phase field simulation gives an obvious domain evolution during the annealing process, and the FD configuration of the BTO film with different annealing times is displayed in Figs. 2(d1)–2(d3). Almost no domain exists in the
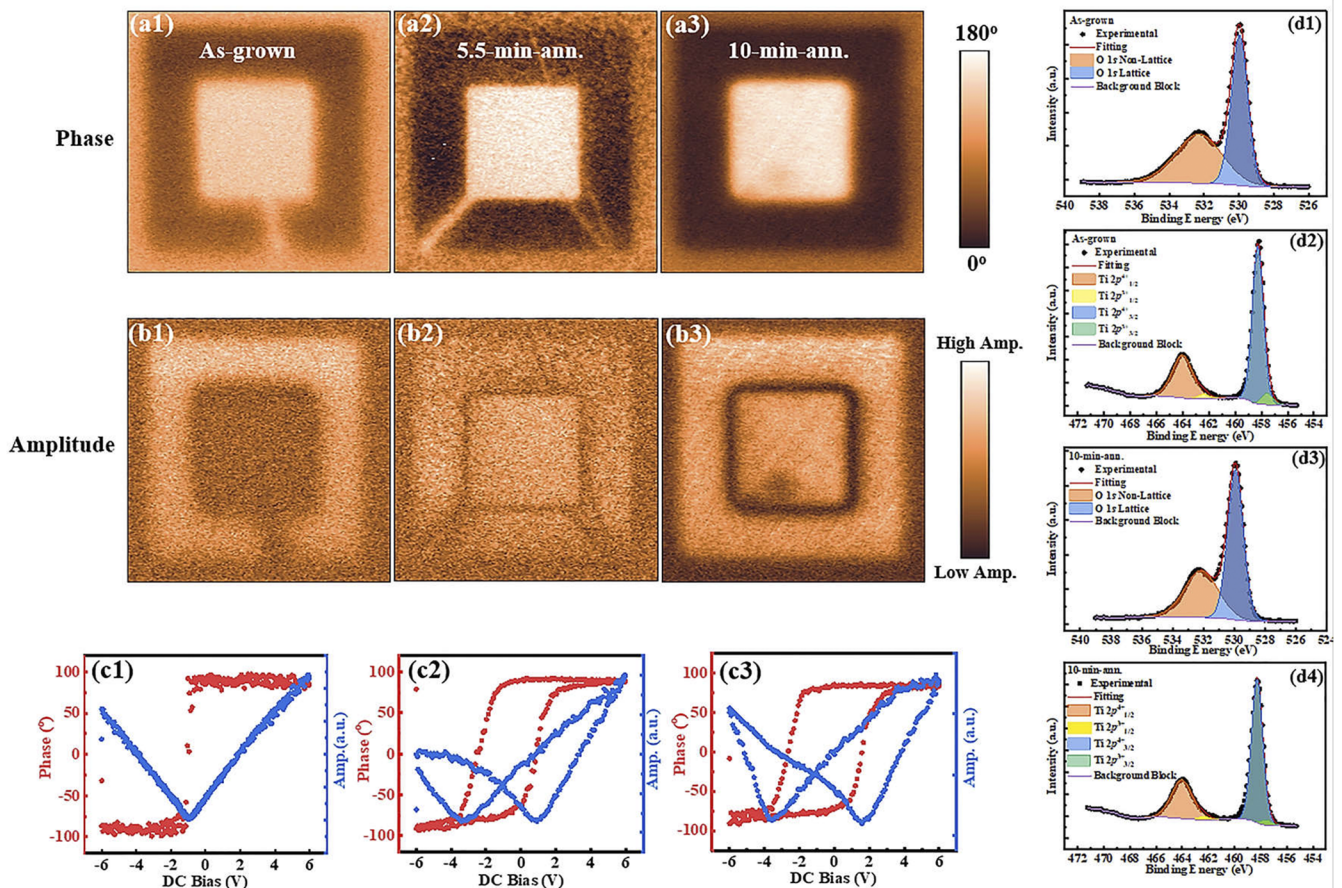
**FIG. 3.** PFM (a1)–(a3) phase images; (b1)–(b3) amplitude images; (c1)–(c3) phase–voltage and amplitude–voltage curves of BTO film with an annealing time of 0, 5.5, and 10 min, respectively; XPS spectra of (d1) O 1s core level in the as-grown BTO film; (d2) Ti 2p core level in the as-grown BTO film; (d3) O 1s core level in BTO with an annealing time of 10 min; and (d4) Ti 2p core level in BTO with an annealing time of 10 min.

as-grown film, especially in the bottom layer, because of the high oxygen vacancy concentration. After 5.5-min-annealing, the domain started to form, and due to the TRRs' existence, the domain size in the bottom layer is quite smaller than that in the bulk layer. In the relaxed regions of the 10-min-annealing film, normal-sized domains formed regardless of the height of the film. From this result, we can assume that the ferroelectric domain forms during the annealing process rather than the deposition process of the PLD technique.

Along with such a lattice transformation, the films' ferroelectricity and the corresponding bottom layers (8-nm BTO) were characterized through piezoresponse force microscopy (PFM). The phase and amplitude images with the phase–voltage and amplitude–voltage loops of films annealed at different times are shown in Fig. 3 after a bias voltage of −6 V (2×2 μm^2) and then +6 V (1×1 μm^2). The same information of bottom-layer-BTO is displayed in Fig. S6 with the same writing configuration under ± 3 V. The contrast in phase image increases with increasing annealing time as shown in Figs. 3(a1)–3(a3), and as shown in Figs. 3(b1)–3(b3), the boundary between different switching squares in amplitude images, which is typically regarded to be the canceling contribution of opposite domain wall,[27,28] becomes sharper. This demonstrates the FD growth of BTO-s during the annealing process with oxygen vacancies being filled, which can also be proved by the phase–voltage and amplitude–voltage loops as shown in Figs. 3(c1)–3(c3), in which the E_C increases from ~0 to 2.5 V with increasing time. Here, the author would like to emphasize that even though the contrast in the PFM phase image can be observed in all the BTO films with different annealing times, the existence of domain switching behavior can only be confirmed in

5.5-min annealing and 10-min annealing ones, for the lack of amplitude minimum in the boundary between different squares.[29] The FD switching behavior of the 8-nm BTO strained layer is similar to its thicker counterparts. As shown in Fig. S6, a sharp boundary can also be distinguished in the amplitude image in a 10-min-annealing one and becomes diffused in the films with a shorter annealing time. The XPS spectra were recorded for the Ti-2p and O-1s core levels in the BTO film to confirm the oxygen vacancy-filling process with annealing times of 0 and 10 min. The peaks at 530 and 532 eV in Figs. 3(d1) and 3(d3) are attributed to lattice-O and non-lattice-O (−OH absorbed on the film surface), respectively. The peaks for Ti 2p3/2 and Ti 2p1/2 at 458.3 and 464.1 eV can be fitted by two peaks, corresponding to Ti^{4+} and Ti^{3+}, according to the Gaussian–LorenCross function. The decreasing intensity of the peaks for Ti^{3+} in Figs. 3(d2) and 3(d4) shows strong evidence of the decrement of oxygen vacancy during the annealing process.

100-nm-thick Pt with a side length of 100 μm was patterned on BTO as top electrodes, as sketched in Fig. S7(a). We took I–V measurements for these films from −8 to 8 V, and the result is plotted in Fig. 4(a). The curve's downward shift reveals the film's increasing resistance with increasing annealing time, and the shape of the curve changes from a symmetrical butterfly to an asymmetrical one with hysteresis on the positive side. For a deeper analysis, the three curves were all fitted based on the relationship of $\log A$ ~ $\log V$ and $\log A$ ~ $V^{1/2}$, as illustrated in Figs. 4(b1) and 4(b2), respectively. The slope of the previous relationship is 1.05 and 1.96 for the as-grown and 5.5-min-annealing BTO, signifying an Ohmic conduction and space-charge-limited current (SCLC) conduction, respectively.[30] In contrast, such a relationship in 10-min-annealing
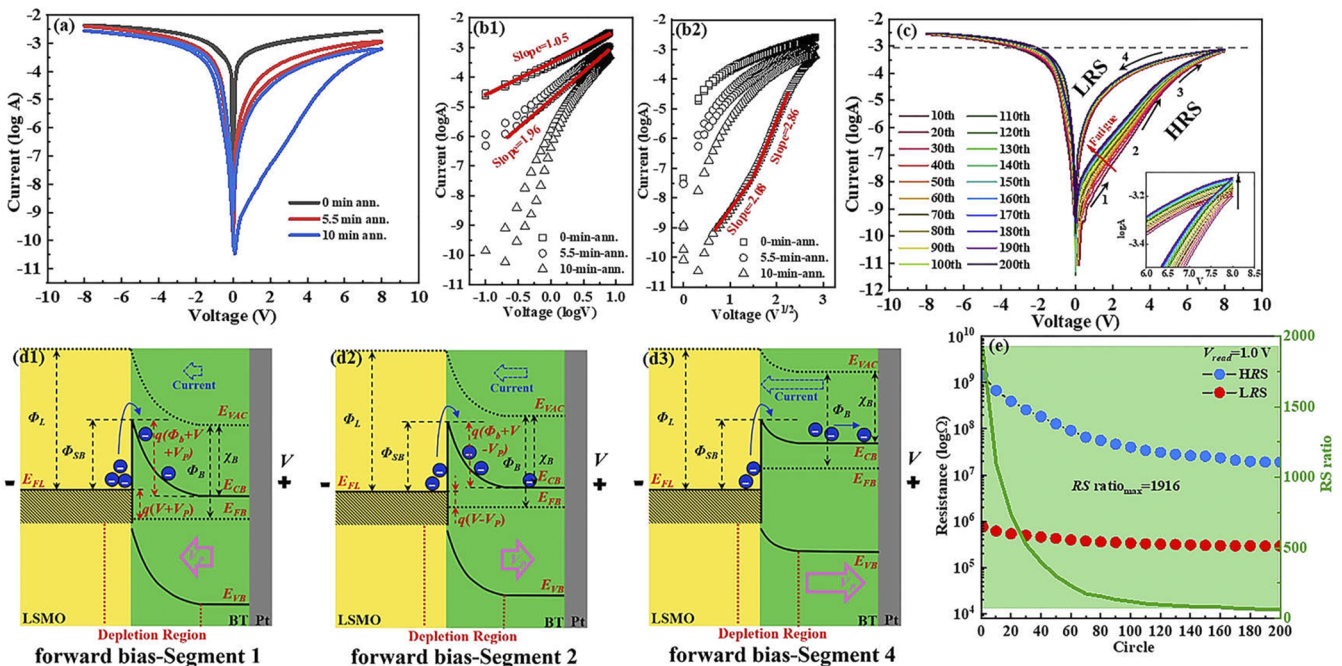
FIG. 4. (a) I–V curves of BTO with annealing times of 0, 5.5, and 10 min; fitting result of BTO with annealing times of 0, 5.5, and 10 min according to the relationship between (b1) $\log A$ and $\log V$; (b2) $\log A$ and $V^{1/2}$; (c) I–V curves during 200 cycles with ten-circle-gap of 10-min-annealing BTO; (d1)–(d3) band diagram analysis on the BTO/LSMO interface of segment 1, segment 2 or 3, and segment 4, respectively, in (c); and (e) resistance values extracted at 1.0 V from (c) and the corresponding RS ratio.

BTO cannot be linearly fitted. On the contrary, a linear relationship was only obtained in 10-min-annealing BTO according to the latter relationship with slopes of 2.08 and 2.86 in two different voltage ranges, indicating an FD-modulated Schottky emission.[30,31] A conclusion from the dielectric behavior also shows some evidence for the existence of Schottky emission in the LSMO/BT interface by confirming the oxygen-deficient property (*as shown in the supplementary material*).[32–35] Figure 4(c) displays the I–V variation in 10-min-annealing BTO during 200 circles with a ten-circle gap. An obvious upward shift from 0 to 2 V in the curve with increasing cycle number is seen, and all the curves can be divided into four segments. With the help of the band diagram, we can clearly understand the formation of the Schottky barrier. (*The definition of the abbreviations is explained in* Fig. S8.) Because the oxygen-deficient BT is an *n*-type semiconductor with the majority of carriers being electrons, the LSMO work function is larger than the BT affinity; the electrons migrated from BT to LSMO after contact.[36–38] A band diagram bending happened and resulted in the formation of a depletion region and a built-in potential (Φ_b), as shown in Figs. S8(c1) and S8(c2), respectively. The band diagrams of both 0-min-ann. BTO and 5.5-min-ann. BTO are also sketched in Figs. S8(a1), S8(a2), S8(b1), and S8(b2), respectively. These band diagrams show that Φ_b starts to form at 5.5 min, and the conducting mechanism transformation occurred at 10 min. When applying a slight forward bias (V) smaller than E_C, both V and the inner voltage caused by the already established polarization (V_P) had the same direction as Φ_b. Thus, E_{FB} decreased, and the built-in potential was increased to ($\Phi_b + V + V_P$), as displayed in Fig. 4(d1). In this case, the electron migration from BT to LSMO was blocked, and only a small amount of electrons in LSMO could overcome Φ_b, resulting in a very low current (*segment* 1). When the forward bias increased above E_C, the already established polarization was switched, so the built-in potential was decreased to ($\Phi_b + V - V_P$), and a higher current was thus obtained[39] (*segment* 2). After the domains were completely switched, further increasing the voltage will not increase the polarization, so the current increment slows down again, as seen in segment 3. The upward shift behavior receded at this moment, for the FD switching effect decreased at the higher voltage.[40] Segments 1–3 are considered a high resistance state (HRS). During voltage ramping down, as seen in segment 4, the conduction was dominated by the polarization coupled trap emptying limited conduction, resulting in a low resistance state (LRS),[31] as shown in Fig. 4(d3). The endurance

performance for up to 200 cycles measured at V_{read} = 1.0 V for 10-min-annealing BTO is shown in Fig. 4(e), and a resistive switching (*RS*) ratio range of 1916 to 198 is obtained. Because of the FD modulation, the *RS* ratio below E_c is much higher than in the other voltage ranges, as shown in Fig. S9. Table I shows the comparison of the *RS* ratio of some typical BT-based devices with that of our work, and our work has a significant advantage in applying memory devices over other BT-based materials.

In summary, the *loss-and-reappearance* phenomenon of BTO interfacial was revealed entirely, which resulted from an ordered–unordered–ordered lattice transformation during the oxygen vacancies' filling process. The FD formation was confirmed to occur in the annealing process. 10-min-annealing BTO exhibited a high RS ratio of up to 1916@1.0 V due to the FD-modulated built-in potential caused by the electron migration, providing a conceptual basis for ferroelectric memristors.

The supplementary material provides the additional phase and structure measurement and the details for the formation of the Schottky barrier.

AUTHOR DECLARATIONS
Conflict of Interest

The authors have no conflicts to disclose.

Author Contributions

Zixiong Sun: Conceptualization (equal); Formal analysis (equal); Methodology (equal); Writing – original draft (equal); Writing – review & editing (equal). **Sizhao Huang**: Data curation (equal); Formal analysis (equal); Methodology (equal); Writing – original draft (equal). **Wenxuan Zhu**: Data curation (equal); Writing – original draft (equal). **Yorick A. Birkhölzer**: Writing – original draft (equal). **Xing Gao**: Methodology (equal). **Romar Angelo Avila**: Data curation (equal). **Houbing Huang**: Supervision (equal); Writing – review & editing (equal). **Xiaojie Lou**: Writing – review & editing (equal). **Evert P. Houwman**: Writing – review & editing (equal). **Minh D. Nguyen**: Supervision (equal); Writing – review & editing (equal). **Gertjan Koster**: Funding acquisition (equal); Supervision (equal); Writing – review & editing (equal). **Guus Rijnders**: Funding acquisition (equal); Supervision (lead); Writing – review & editing (equal).

DATA AVAILABILITY

The data that support the findings of this study are available within the article and its supplementary material and from the corresponding authors upon reasonable request.

TABLE I. Comparison of the *RS* ratio of some typical BT-based devices with that of our work. The V_{read} means the read voltage applied on the device and the *RS* ratio represents the resistive switching ratio.

Structure	V_{read} (V)	*RS* ratio	Reference	Year
BTO/LSMO	0.5	18	41	2021
BTO/Au/LSMO	2.2	70	42	2014
BTO/SNO	0.2	100	43	2019
BTO/LSMO/BTO	0.1	100	44	2019
BTO/LNO	1	170	45	2019
BTO/Nb:STO	0.38	1000	46	2022
BTO/LSMO	**1**	**1916**	**This work**	**2023**
Nb:BTO/SRO	−3	2000	47	2017

REFERENCES

[1] J. F. Scott, "Applications of modern ferroelectrics," Science 315, 954–959 (2007).

[2] R. Waser and M. Aono, "Nanoionics-based resistive switching memories," Nat. Mater. 6, 833–840 (2007).

[3] J. M. Hu, L. Q. Chen, and C. W. Nan, "Multiferroic heterostructures integrating ferroelectric and magnetic materials," Adv. Mater. 28, 15–39 (2016).

[4] L. W. Martin and A. M. Rappe, "Thin-film ferroelectric materials and their applications," Nat. Rev. Mater. 2, 16087 (2017).

[5] J. G. Bell, T. Graule, and M. Stuer, "Barium titanate-based thermistors: Past achievements, state of the art, and future perspectives," Appl. Phys. Rev. 8, 031318 (2021).

[6] Y. Bai, T. Ouyang, Q. Guo, Y. Ning, J. Liu, H. Wei, K. Du, H. Jing, Y. Tian, Y. Pu, and Y. P. Pu, "Achieving ultrahigh energy storage density in super relaxor BCZT-based lead-free capacitors through multiphase coexistence," Appl. Phys. Lett. 122, 263904 (2023).

[7] Y. J. Su, C. X. Chen, H. Pan, Y. Yang, G. R. Chen, X. Zhao, W. X. Li, Q. C. Gong, G. Z. Xie, Y. H. Zhou, S. L. Zhang, H. L. Tai, Y. D. Jiang, and J. Chen, "Muscle fibers inspired high-performance piezoelectric textiles for wearable physiological monitoring," Adv. Funct. Mater. 31, 2010962 (2021).

[8] Z. X. Sun, Z. Wang, Y. Tian, G. Wang, W. Wang, M. D. Yang, X. Y. Wang, F. H. Zhang, and Y. Pu, "Progress, outlook, and challenges in lead-free energy-storage ferroelectrics," Adv. Electron. Mater. 6, 1900698 (2020).

[9] Z. X. Sun, Y. H. Bai, J. Q. Liu, G. Jian, C. Guo, L. Zhang, and Y. Pu, "Interface engineering in ferroelectrics: From films to bulks," J. Alloys Compd. 909, 164735 (2022).

[10] J. L. Lin, R. He, Z. X. Lu, Y. Lu, Z. M. Wang, Z. C. Zhong, X. Zhao, R. W. Li, Z. D. Zhang, and Z. J. Wang, Acta Mater. 199, 9–18 (2020).

[11] Z. X. Sun, J. Q. Liu, H. S. Wei, Q. Guo, Y. H. Bai, S. B. Zhao, S. T. Wang, L. Li, Y. T. Zhang, Y. Tian, X. H. Zhang, H. M. Jing, Y. P. Pu, and S. F. Zhang, "Ultrahigh energy storage capacity in multilayer-structured cellulose-based dielectric capacitors caused by interfacial polarization-coupled Schottky barrier height," J. Mater. Chem. A 11, 20089–20101 (2023).

[12] D. Kan and Y. Shimakawa, "Controlled cation stoichiometry in pulsed laser deposition-grown $BaTiO_3$ epitaxial thin films with laser fluence," Appl. Phys. Lett. 99, 081907 (2011).

[13] Z. P. Li, Z. Y. Zhang, J. Liu, R. X. Zhu, B. Ge, Y. Li, X. Zhang, P. Gao, D. Wang, X. Xu, W. Tian, Y. Jiang, and Y. Jiang, "Enhancement of interfacial polarization in $BaTiO_3$ thin films via oxygen inhomogeneity," Adv. Electron. Mater. 8, 2100876 (2022).

[14] Z. B. Yan, Y. Y. Guo, G. Q. Zhang, and J. M. Liu, "High-performance programmable memory devices based on Co-doped $BaTiO_3$," Adv. Mater. 23, 1351–1355 (2011).

[15] D. Lee, S. H. Baek, T. H. Kim, J. G. Yoon, C. M. Folkman, C. B. Eom, T. W. Noh, and T. W. Noh, "Polarity control of carrier injection at ferroelectric/metal interfaces for electrically switchable diode and photovoltaic effects," Phys. Rev. B 84, 125305 (2011).

[16] A. Molinari, R. Witte, K. K. Neelisetty, S. Gorji, C. Kübel, I. Münch, F. Wöhler, L. Hahn, S. Hengsbach, K. Bade, H. Hahn, and R. Kruk, "Configurable resistive response in $BaTiO_3$ ferroelectric memristors via electron beam radiation," Adv. Mater. 32, 1907541 (2020).

[17] J. F. Yu, M. Yang, J. X. Zhang, Q. J. Ge, A. Zimina, T. Pruessmann, L. Zheng, J. D. Grunwaldt, and J. Sun, "Stabilizing Cu^+ in Cu/SiO_2 catalysts with a shattuckite-like structure boosts CO_2 hydrogenation into methanol," ACS Catal. 10, 14694–14706 (2020).

[18] X. X. Meng, Z. F. Bi, P. Lou, and G. Shang, "Shang tracking electrochemical-cycle-induced surface structure evolutions of cathode material $LiMn_2O_4$ with improved operando Raman spectroscopy," Langmuir 38, 3887–3895 (2022).

[19] R. I. Pelzel, L. A. Zepeda-Ruiz, B. Z. Nosho, Y. Li, W. H. Weinberg, and D. Maroudas, "Mechanical behavior of thin buffer layers in InAs/GaAs(111)A heteroepitaxy," Appl. Phys. Lett. 76, 3017–3019 (2000).

[20] J. Sigmund, D. Pavlidis, H. L. Hartnagel, N. Benker, and H. Fuess, "Nonstoichiometric growth and cluster formation in low temperature grown GaAsSb for terahertz-applications," J. Vac. Sci. Technol., B: Microelectron. Nanometer Struct.-Process., Meas., Phenom. 24, 1556–1558 (2006).

[21] T. Gladkikh, A. Kozlovskiy, K. Dukenbayev, and M. Zdorovets, "Radiation resistance of AlN ceramics as a result of irradiation with low-energy C^{2+} ions," Mater. Charact. 150, 88–97 (2019).

[22] H. Muta, K. Kurosaki, and S. Yamanaka, "Thermoelectric properties of doped $BaTiO_3$–$SrTiO_3$ solid solution," J. Alloys Compd. 368, 22–24 (2004).

[23] H. P. Sun, W. Tian, X. Q. Pan, J. H. Haeni, and D. G. Schlom, "Evolution of dislocation arrays in epitaxial $BaTiO_3$ thin films grown on (100) SrTiO3," Appl. Phys. Lett. 84, 3298 (2004).

[24] S. Y. Choi, S. D. Kim, M. Choi, H. S. Lee, J. Ryu, N. Shibata, T. Mizoguchi, E. Tochigi, T. Yamamoto, S. J. L. Kang, and Y. Ikuhara, "Assessment of strain-generated oxygen vacancies using $SrTiO_3$ bicrystals," Nano Lett. 15, 4129–4134 (2015).

[25] J. M. Börgers, J. Keller, K. Ran, E. Larenz, T. E. Weirich, R. R. Dittmann, and A. De Souza, "Faster diffusion of oxygen along dislocations in (La, Sr)$MnO_{3+\delta}$ is a space-charge phenomenon," Adv. Funct. Mater. 31, 2105647 (2021).

[26] S. Stich, K. Ding, Q. K. Muhammad, L. Porz, C. Minnert, W. Rheinheimer, K. Durst, J. Rödel, T. Frömling, and X. F. Fang, "Room-temperature dislocation plasticity in $SrTiO_3$ tuned by defect chemistry," J. Am. Ceram. Soc. 105, 1318–1329 (2022).

[27] Y. Ivry, D. P. Chu, J. F. Scott, and C. Durkan, "Flux closure vortexlike domain structures in ferroelectric thin films," Phys. Rev. Lett. 104, 207602 (2010).

[28] N. Balke, P. Maksymovych, S. Jesse, A. Herklotz, A. Tselev, C. B. Eom, I. I. Kravchenko, P. Yu, and S. V. Kalinin, "Differentiating ferroelectric and nonferroelectric electromechanical effects with scanning probe microscopy," ACS Nano 9, 6484–6492 (2015).

[29] Z. Guan, Z. Z. Jiang, B. B. Tian, Y. P. Zhu, P. H. Xiang, N. Zhong, C. G. Duan, and J. H. Chu, "Identifying intrinsic ferroelectricity of thin film with piezoresponse force microscopy," AIP Adv. 7, 095116 (2017).

[30] F. C. Chiu, "A review on conduction mechanisms in dielectric films," Adv. Mater. Sci. Eng. 2014, 578168.

[31] A. P. Chen, W. R. Zhang, L. R. Dedon, D. Chen, F. Khatkhatay, J. L. MacManus-Driscoll, H. Wang, D. Yarotski, J. Chen, X. Gao, L. W. Martin, A. Roelofs, and Q. Jia, "Couplings of polarization with interfacial deep trap and Schottky interface controlled ferroelectric memristive switching," Adv. Funct. Mater. 30, 2000664 (2020).

[32] S. Steinsvik, R. Bugge, J. Gjonnes, J. Tafto, and T. Norby, "The defect structure of $SrTi_{1-x}Fe_xO_{3-y}$ ($x = 0$–0.8) investigated by electrical conductivity measurements and electron energy loss spectroscopy (EELS)," J. Phys. Chem. Solids 58, 969 (1997).

[33] G. C. Lin, H. Liu, and J. X. Zhang, "Oxygen vacancy relaxation in $Ca_3Co_4O_{9+\delta}$ Ceramics," Solid State Phenom. 184, 98–103 (2012).

[34] T. F. Zhang, X. G. Tang, Q. X. Liu, S. G. Lu, Y. P. Jiang, X. X. Huang, and Q. F. Zhou, "Oxygen-vacancy-related relaxation and conduction behavior in $(Pb_{1-x}Ba_x)(Zr_{0.95}Ti_{0.05})O_3$ ceramics," AIP Adv. 4, 107141 (2014).

[35] S. Saha and T. P. Sinha, "Low-temperature scaling behavior of $BaFe_{0.5}Nb_{0.5}O_3$," Phys. Rev. B 75, 069901 (2007).

[36] A. R. Calzada, F. Gallego, Y. Kalcheim, P. Salev, J. del Valle, I. Tenreiro, C. Leon, J. Santamaria, and I. K. Schuller, "Switchable optically active Schottky barrier in $La_{0.7}Sr_{0.3}MnO_3$/$BaTiO_3$/ITO ferroelectric tunnel junction," Adv. Electron. Marer. 7, 2100069 (2021).

[37] X. Chen, C. H. Jia, Y. H. Chen, G. Yang, and W. F. Zhang, "Ferroelectric memristive effect in $BaTiO_3$ epitaxial thin films," J. Phys. D: Appl. Phys. 47, 365102 (2014).

[38] P. Singh, P. K. Rout, M. Singh, R. K. Rakshit, and A. Dogra, "Thickness dependent charge transport in ferroelectric $BaTiO_3$ heterojunctions," J. Appl. Phys. 118, 114103 (2015).

[39] M. A. Lampert, "Simplified theory of space-charge-limited currents in an insulator with traps," Phys. Rev. 103, 1648 (1956).

[40] D. H. Do, P. G. Evans, E. D. Isaacs, D. M. Kim, C. B. Eom, and E. M. Dufresne, "Structural visualization of polarization fatigue in epitaxial ferroelectric oxide devices," Nat. Mater. 3, 365–369 (2004).

[41] N. Jedrecy, V. Jagtap, C. Hebert, L. Becerra, D. Hrabovsky, A. Barbier, and X. Portier, "Resistive switching and redox process at the $BaTiO_3$/(La, Sr)MnO_3 multiferroic-type interface," Adv. Electron. Mater. 7, 2000723 (2021).

13 November 2023 14:23:14

[42] D. Chu, X. Lin, A. Younis, C. M. Li, F. Dang, and S. Li, "Growth and self-assembly of BaTiO$_3$ nanocubes for resistive switching memory cells," J. Solid State Chem. **214**, 38–41 (2014).

[43] M. X. Jia, Z. Q. Ren, Y. D. Liu, Y. Cheng, R. Huang, P. H. Xiang, X. D. Tang, B. B. Tian, N. Zhong, and C. G. Duan, "Ferroelectric polarization-controlled resistive switching in BaTiO$_3$/SmNiO$_3$ epitaxial heterostructures," Appl. Phys. Lett. **114**, 102901 (2019).

[44] D. Lu, S. Crossley, R. Xu, Y. Hikita, and H. Y. Hwang, "Freestanding oxide ferroelectric tunnel junction memories transferred onto silicon," Nano Lett. **19**, 3999–4003 (2019).

[45] X. Wang, M. Wu, F. S. Wei, Y. T. Zhang, C. Y. Zheng, X. J. Lou, S. J. Pennycook, and Z. Wen, "Electroresistance of Pt/BaTiO$_3$/LaNiO$_3$ ferroelectric tunnel junctions and its dependence on BaTiO$_3$ thickness," Mater. Res. Express **6**, 046307 (2019).

[46] Y. D. Zhu, M. Zhao, Y. Zhang, T. Zhang, and H. Zhou, "Resistive switching and photovoltaic response characteristics for the BaTiO$_3$/Nb: SrTiO$_3$ heterostructure," Appl. Phys. Lett. **120**, 103504 (2022).

[47] Q. Jin, C. Y. Zheng, Y. C. Zhang, C. J. Lu, J. Y. Dai, and Z. Wen, "Enhanced resistive memory in Nb-doped BaTiO$_3$ ferroelectric diodes," Appl. Phys. Lett. **111**, 032902 (2017).

13 November 2023 14:23:14